

Multiple crossovers and coherent states in a Mott-Peierls insulatorO. Nájera,¹ M. Civelli,¹ V. Dobrosavljević,² and M. J. Rozenberg^{1,3}¹*Laboratoire de Physique des Solides, CNRS-UMR8502, Université Paris-Sud, Orsay 91405, France*²*Department of Physics and National High Magnetic Field Laboratory, Florida State University, Tallahassee, Florida 32306, USA*³*Department of Physics, University of California San Diego, 9500 Gillman Dr., La Jolla, California 92093, USA*

(Received 30 July 2017; revised manuscript received 16 October 2017; published 9 January 2018)

We consider the dimer Hubbard model within dynamical mean-field theory to study the interplay and competition between Mott and Peierls physics. We describe the various metal-insulator transition lines of the phase diagram and the breakdown of the different solutions that occur along them. We focus on the specific issue of the debated Mott-Peierls insulator crossover and describe the systematic evolution of the electronic structure across the phase diagram. We found that at low intradimer hopping, the emerging local magnetic moments can unbind above a characteristic singlet temperature T^* . Upon increasing the interdimer hopping, subtle changes occur in the electronic structure. Notably, we find Hubbard bands of a mix character with coherent and incoherent excitations. We argue that this state might be relevant for materials such as VO_2 and its signatures may be observed in spectroscopic studies, and possibly through pump-probe experiments.

DOI: [10.1103/PhysRevB.97.045108](https://doi.org/10.1103/PhysRevB.97.045108)**I. INTRODUCTION**

Vanadates are fascinating materials that provide a fertile playground to study nontrivial phase transitions driven by the electronic correlation. Their structures follow the Magnéli series $\text{V}_n\text{O}_{2n-1}$ and most of them exhibit insulator-to-metal transitions (IMT) upon heating. Significantly, these transitions involve a structural change but are disconnected to magnetic ordering, with the exception of the most famous members of the series V_2O_3 and VO_2 . In the former, the magnetic and structural transitions occur at the same temperature, while in the latter there is a structural transition but no magnetic ordering at any temperature.

Vanadium dioxide is particularly appealing because its transition occurs close to room temperature, around 340 K, so it may enable practical applications in novel electronic devices [1,2]. In fact, the study of this material is receiving a great deal of attention. Therefore, a basic understanding of the nature of its electronic state and its insulator-to-metal transition (IMT) is of great importance.

VO_2 may be considered a realization of a Mott system, as it has only one electron per vanadium atom which should lead to a partially filled band. However, since it exhibits a nonmagnetic insulating ground state, this classification has often been challenged. In fact, in influential early papers, Goodenough [3,4] argued that the first-order IMT occurs concomitant with a structural distortion of the vanadium chains in the crystal, so the gap opening upon cooling should be due to a Peierls lattice instability. Density functional theory (DFT) calculations made significant progress trying to substantiate Goodenough's claim [5,6], however, the nature of the insulating state and the IMT in VO_2 still remains a puzzle. The development of methods that incorporate strong correlation effects in realistic lattice calculations provided additional light. Eventually, Biermann *et al.* showed using cluster dynamical mean-field theory (CDMFT) with DFT that strong correlations due to local Coulomb

repulsion may lead to the opening of a gap [7,8]. Hence, the ground state was considered a “Peierls insulator with dynamical correlations.” This theoretical problem continued to attract theoretical attention as the numerical techniques were further improved. Weber *et al.* [9] argued that the mechanism driving the insulator state was better characterized as a “Peierls assisted orbitally selective Mott transition.” They observed that mainly the a_{1g} orbital drives the opening of the gap. A more recent study where the oxygen atoms were explicitly included [10] enabled a more comprehensive account of the various phases observed in VO_2 . However, it also led to the reinterpretation of the transition as a “Mott transition in the presence of strong intersite exchange.” We should also mention here the work by Eyert, whose calculations including correlations through hybrid functionals [11] may also open a gap in the monoclinic phase.

While the technical improvements of the computational methods of realistic correlated materials made significant steps forward in our understanding of the electronic states, it is also true that their technical complexity represents a challenge. For instance, despite multiple studies dedicated to this material [7,9,10,12], some basic issues remain unaccounted for, such as the existence of a first-order thermally driven insulator-metal transition just above room temperature. Finite-temperature studies are in principle beyond the applicability of DFT methods although we should point out the recent work of Plašienka *et al.* [13]. We investigated the issue of a first-order IMT in a recent paper [14] employing a model Hamiltonian approach within CDMFT. Although the model is rather schematic, namely, a lattice of correlated dimers, it was intended to qualitatively capture the dimerization-delocalization competition in the monoclinic phase of VO_2 . We showed that there is a thermally driven first-order Mott transition that occurs at a temperature range compatible with the experimental observation. Moreover, we have also provided an interpretation to the puzzling presence of a mid-infrared peak in the optical

conductivity of metallic nanosize islands observed during the transition [15] in terms of a novel correlated “monoclinic” metal [14]. Model Hamiltonians that may capture the key ingredients are also attractive for experimentalist as they provide useful insights within a more intuitive yet nontrivial physical framework for strongly interacting systems.

In this paper we continue with this strategy and make inroads into the investigation of the nature of the insulator and metallic states realized in the dimer Hubbard model (DHM) within CDMFT. Specifically, we address the issue on the physical characterization of the insulator state. A key feature of our approach is to observe that the quantum impurity problem of the DHM has the same form as the respective quantum impurity problem of the DFT+CDMFT method on realistic lattices. In fact, we shall see that our model solution does capture in a simpler context several features already seen in DFT+CDMFT studies [8,16], such as the presence of renormalized coherent bands in the insulator.

The model Hamiltonian approach enables the systematic investigation of the whole parameter space, which sheds light on the interplay of physical mechanisms. We shall address the question of the physical crossover from a pure Peierls insulator, which is a band insulator of a lattice of dimers without correlations, to the pure (un-dimerized) correlated Mott insulator. We shall see that the behavior of the system across the crossover regime is nontrivial. One of our main results is that as the system evolves from the Mott to the Peierls insulator, there are at least four different regimes, including an unprecedented state where the Hubbard bands have an electronic structure with mixed coherent and incoherent character. Interestingly, VO_2 could be in this peculiar regime, which might eventually be seen in spectroscopy experiments. On the other hand, we also investigated the correlated “monoclinic” metallic state and show that it can be understood in simple terms as a renormalized two-band heavy metal at low frequencies. Interestingly, indications of a monoclinic metal in VO_2 have been reported in several experimental studies [17–24].

In a larger perspective, our systematic investigation of the model parameter space should also shed light for the classification of a variety of monoclinic transition-metal oxide systems with the MO_2 formula [25] and the nonmagnetic insulator states of other vanadates.

This paper is organized as follows: In Sec. II we introduce the DHM and the DMFT equations. We also describe a simple parametrization of a renormalized two-band model that will be useful for the discussion of our results. In Sec. III we present the phase diagram and discuss the various insulator-metal transitions of the model. In particular, we describe the destruction of the correlated metal and the insulator in the Mott regime. In Sec. IV we present the detailed study of the Mott to Peierls crossover. We characterize the several distinct physical regimes, including one with mixed coherent and incoherent features in the Hubbard bands possibly relevant for VO_2 . Section V is dedicated to the conclusions of our work.

II. DIMER HUBBARD MODEL

We focus on the dimer Hubbard model, which is a basic and natural extension of the single-band Hubbard model. The

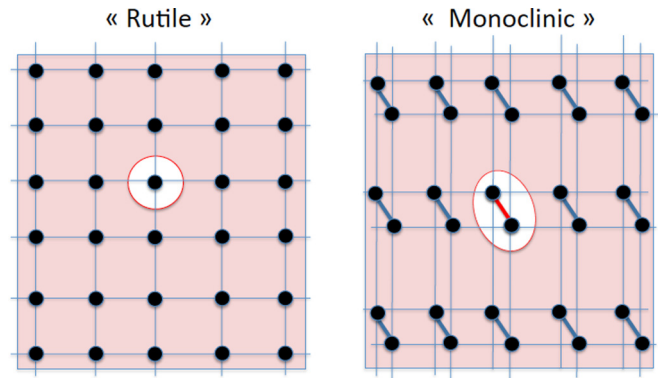


FIG. 1. Schematic representation of the higher-symmetry “rutile” lattice with one atom per unit cell and the low-symmetry “monoclinic” lattice, which is a lattice of dimers. In shaded red, we represent the quantum impurity effective environment determined through the CDMFT equations. Notice that our model is defined on a semicircular noninteracting density of states, that may be realized in a Bethe lattice. Nevertheless, here we depict a square lattice just for the sake of simplicity.

DHM reads as

$$H = \left[-t \sum_{\langle i,j \rangle \alpha \sigma} c_{i\alpha\sigma}^\dagger c_{j\alpha\sigma} + t_\perp \sum_{i\sigma} c_{i1\sigma}^\dagger c_{i2\sigma} + \text{H.c.} \right] + U \sum_{i\alpha} n_{i\alpha\uparrow} n_{i\alpha\downarrow}, \quad (1)$$

where $\langle i, j \rangle$ denotes nearest-neighbor lattice cells, $\alpha = \{1, 2\}$ denote the dimer orbitals within a given cell, σ is the spin, t is the lattice (i.e., interdimer) hopping, and (t_\perp) is the intradimer hopping. The parameter U is the onsite Coulomb repulsion.

The noninteracting limit of the DHM has two bands which are locally hybridized at every lattice cell site. This leads to the parallel splitting of the two bands by $2t_\perp$. When this splitting is large enough, the system has a continuous metal-insulator transition. We associate this to a Peierls-type mechanism, as it is driven by the increase of the intradimer hopping amplitude t_\perp . It can be ascribed to a schematic representation of the monoclinic distortion in the real material that creates dimers in the unit cell (see Fig. 1). Another way to see this IMT is by starting from the $t \rightarrow 0$ limit, where the local dimers that form a bonding (B) and an antibonding (AB) molecular orbital at every 1-2 link. Switching on the interdimer hopping, these orbitals lead to an insulating state with two split flat bands. At a large enough (lattice-geometry-dependent) value of t , the B and AB bands start to overlap and realize a transition into a metal.

Before proceeding, we should avoid any confusion here by noting that the model (1) is fully defined only after its lattice is specified. For instance, if dimers are arranged as a one-dimensional system, the model is a “ladder” (the dimer rungs are perpendicular to the direction of the lattice). In two dimensions, as in the schematic Fig. 1, one would get a “bilayer” model, where the dimer rungs connect at every site two parallel 2D layers. Those systems have qualitatively different behaviors from the one that concerns us here. In 3D systems that have strong local interactions, one may expect the dynamical mean

field theory (DMFT) to be a reasonable approximation [26]. In fact, DFT+DMFT methods are implicitly based on such an assumption. The DMFT approach to the DHM with a dimer unit cell is, strictly speaking, a cluster-DMFT calculation, possibly the simplest instance of CDMFT. In DMFT and CDMFT, it is mathematically convenient and thus customary to adopt a noninteracting semicircular density of states (DOS), which is realized in a Bethe lattice [26]. In addition, such a DOS qualitatively resembles that of a three-dimensional lattice system. In fact, it has a finite bandwidth given by $4t$ defined in Eq. (1). As in previous works, we adopt as unit of energy the half-bandwidth $D = 2t = 1$. We should emphasize here that the physics of models treated within DMFT in general does not depend on specific geometry of the lattice, but on the nature of the quantum impurity problem. As we mentioned already, the realistic VO_2 lattice within DFT+CDMFT has the same type of quantum dimer impurity as in the present case. Our model has the additional simplification of considering one orbital at each site instead of the three in the realistic case. We may see in Fig. 1 schematic “rutile” and “monoclinic” lattices. From our previous discussion, the key feature is that in the former case there is a single site in the unit cell, while in the latter case there is a dimer. The “rutile” lattice can be qualitatively associated to a conventional single-band Hubbard model [26], while the “monoclinic” one can be thought of as two copies of Hubbard models coupled at every unit-cell site by the intradimer hopping t_\perp . In the limit of $t_\perp \rightarrow 0$, the two copies become independent and one recovers the conventional single-site Hubbard model physics [14,26,27]. As an additional remark, here we should say that both the single-site Hubbard and the dimer Hubbard models at half-filling have antiferromagnetic ground states, which are favored in bipartite lattices. Nevertheless, the study of the MITs within the PM (metastable) states is important in its own right as it has been very useful to reveal the physical competition between different correlated states [26].

A. CDMFT equations and the bonding-antibonding basis

The solution of the CDMFT equations is obtained in terms of the one-particle propagators $G_{\alpha,\beta}$ (with $\alpha,\beta = 1,2$), which are subject to the self-consistent condition

$$\mathbf{G}(\omega) = \int d\varepsilon \rho(\varepsilon)[(\omega - \varepsilon)\mathbb{I} - t_\perp \sigma_x - \Sigma(\omega)]^{-1}, \quad (2)$$

where σ_x is the x Pauli matrix and $\Sigma_{\alpha,\beta}$ is the local self-energy. The calculation of the local self-energy requires the solution of the so-called local quantum impurity problem, which is often a generalization of the Kondo problem [26]. To solve such a quantum impurity problem requires the numerical implementation of a many-body approach. Following previous work [14], here we make extensive use of the iterative perturbation theory (IPT) [27] that allows fast and precise calculations in the whole phase diagram and at all T and $T = 0$. Notably, IPT becomes *exact* in the limits of $T = 0$ and $t \rightarrow 0$ or $U \rightarrow 0$, for all t_\perp (see Appendix B) and its numerical precision allows for reliable analytic continuation of the data to the real axis. We also benchmarked our IPT calculations with results from other numerical methods such as the continuous time quantum Monte Carlo (CT-QMC) [28,29] and the exact diagonalization

(ED) [26]. The former is a finite- T calculation and the latter is a $T = 0$ one. These methods are both exact up to systematic errors, but are numerically very expensive and have the serious drawback of requiring, in the case of CT-QMC, the analytic continuation of the (noisy) imaginary axis results.

In the present case of half-filling (i.e., one particle per site), particle-hole symmetry holds. We further assume translational invariance and search for a paramagnetic solution. We have then $G_{11}(\omega) = G_{22}(\omega)$ and $G_{12}(\omega) = G_{21}(\omega)$. The self-energies have similar properties. In order to simplify the discussion of the evolution of the electronic structure, it is convenient to consider the B/AB representation that renders the Green’s functions and self-energies *diagonal*:

$$G_{\text{B/AB}} = G_{11} \mp G_{12}, \quad (3a)$$

$$\Sigma_{\text{B/AB}} = \Sigma_{11} \mp \Sigma_{12}. \quad (3b)$$

In the B/AB basis the electronic structure of the noninteracting problem is particularly simple. The single-particle energies $E_k^{\text{B/AB}}$ form two parallel bands of bandwidth $2D$ and are split by $2t_\perp$, i.e., $E_k^{\text{B/AB}} = \mp t_\perp + \epsilon_k$, where ϵ_k is the single-particle energy of the bands for $t_\perp = 0$. In the present case, since we employ a semicircular DOS (realized in a Bethe lattice in infinite dimensions) the lattice single-particle energies ϵ_k drop their k dependence [26] and then are simply labeled by $\epsilon \in [-D, D]$ [26]. Thus, at finite t_\perp and $U = 0$, the model DOS is composed of two semicircles split by $2t_\perp$, $\rho_{\text{B/AB}}(\omega) = \frac{2}{\pi D^2} \sqrt{D^2 - (\omega \pm t_\perp)^2}$.

B. Renormalized two-band model

In order to better analyze our results in the subsequent sections, it is convenient to introduce here a simple low-energy parametrization of the two-band system. We may think of this as a noninteracting renormalized two-band model (R2B). In a normal (i.e., Fermi liquid) metal the self-energy is well-behaved at low frequencies [30]. In the present case we expand around $\omega = 0$ the self-energies of the mean-field equations (2), and introduce a quasiparticle residue Z :

$$Z^{-1} = 1 - \left. \frac{\partial \text{Re} \Sigma_{\text{B/AB}}(\omega)}{\partial \omega} \right|_0 = 1 - \left. \frac{\partial \text{Re} \Sigma_{11}(\omega)}{\partial \omega} \right|_0 \quad (4)$$

and a renormalized intradimer hopping t_\perp as

$$\tilde{t}_\perp = t_\perp \mp \text{Re} \Sigma_{\text{B/AB}}(\omega)|_0 = t_\perp + \text{Re} \Sigma_{12}(\omega)|_0. \quad (5)$$

The DOS of the R2B model then reads as

$$\rho_{\text{B/AB}}^{\text{R2B}}(\omega) \sim \frac{2}{\pi D^2} \sqrt{D^2 - \left(\frac{\omega}{Z} \pm \tilde{t}_\perp \right)^2} \quad (6)$$

that corresponds to two heavy effective bands with dispersion $E_\epsilon^{\text{B/AB}} = \mp Z \tilde{t}_\perp + Z \epsilon$, where the effective mass renormalization is $m^*/m = 1/Z$. The overlap between the two band edges is given by 2η , where

$$\eta = ZD - Z \tilde{t}_\perp. \quad (7)$$

Thus, for $\eta > 0$ we have a metal state, and for $\eta < 0$ (i.e., splitting dominates) the DOS opens a gap (see Fig. 2). We will use this quantity to describe the metal-to-insulator transition, in the next section.

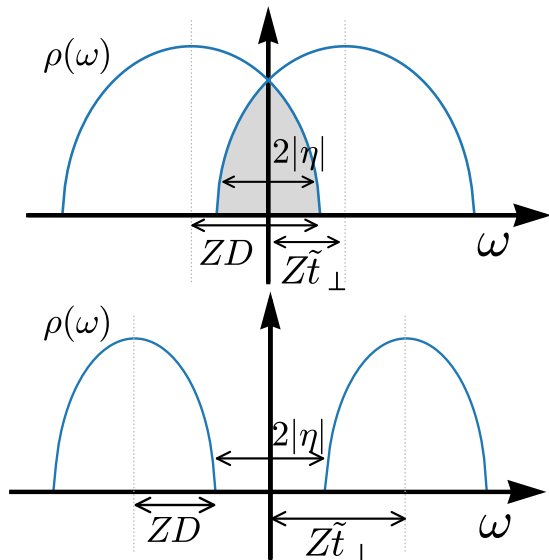


FIG. 2. Schematic representation of the two bands in the R2B model. This model is a simple renormalization of the noninteracting case where $Z = 1$ and the intradimer hopping is $\tilde{t}_\perp = t_\perp$. ZD denotes the renormalization of bandwidth and 2η the overlap of the two bands.

The renormalized two-band (R2B) model may describe both metallic and insulating states, so long as the Σ remains well behaved (i.e., linear) according to the parametrization. As it turns out, the description will be valid at low frequencies throughout the metallic phase, which is a Fermi liquid. In the insulator, we shall see that it is a good approximation only within the Peierls limit, where the interaction and thus the Σ are small. In the Mott regime, this parametrization is not appropriate.

III. PHASE DIAGRAM AND INSULATOR-METAL TRANSITIONS

In Fig. 3 we show the $U - t_\perp$ phase diagram at $T = 0$, which is well known from previous studies [14,27,31,32]. We recall now its main features. There is a metallic phase for $t_\perp < 1$, and an insulator phase at high enough U . The IMT changes character depending on the value of t_\perp . At values higher than $t_\perp \approx 0.7$ the transition is continuous (second order) along a line U_{c_3} indicated in green in Fig. 3. At smaller values of t_\perp , there are two lines U_{c_1} and U_{c_2} , respectively, indicated in blue and red in the figure. These are two spinodal lines of the mean-field theory self-consistent solution. The metal state is destabilized for $U > U_{c_2}$ whereas the insulator state is destabilized along $U < U_{c_1}$. Thus, in-between the two spinodal lines there are two different solutions of the CDMFT equations, one metallic and one insulating. At finite temperature, this coexistence region shrinks, until it disappears at a critical temperature. At higher T there is a crossover behavior and bad metal states [14]. This phase diagram is obtained with IPT but we have validated all its main features by extensive CT-QMC calculations [14].

The description of how these transitions take place in this basic model of strongly correlated systems has (rather surprisingly) not been investigated in detail. As we discussed before, this type of impurity model is at the core of calculations of

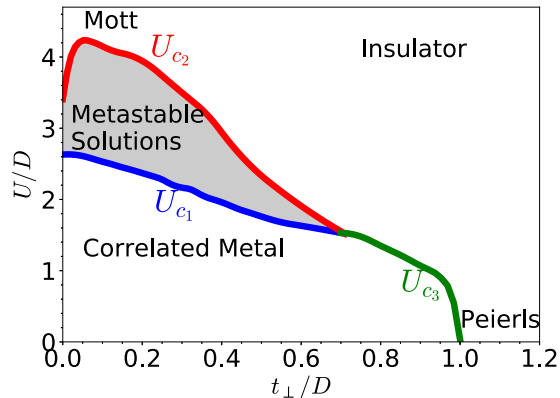


FIG. 3. The metal-insulator transition takes place along the U_{c_1} , U_{c_2} , and U_{c_3} lines (blue, red, and green, respectively). The U_{c_2} line corresponds to a spinodal line where the metallic solution discontinuously disappears upon increasing U . Along the U_{c_3} line there is a continuous second-order metal-insulator transition. The U_{c_1} line marks the spinodal where the Mott insulator vanishes discontinuously upon decreasing U . The Mott insulator is continuously connected to the Peierls insulator, however, different crossover behaviors can be identified.

realistic material with a dimer in the unit cell. We shall therefore describe the transitions in detail in the next subsections.

A. Metal-to-insulator transitions across U_{c_2} and U_{c_3}

The metal-to-insulator transition by increasing U dramatically changes its character as a function of t_\perp . In Fig. 4 we illustrate this by showing the evolution of the frequency-dependent DOS with increasing U , for two representative values $t_\perp = 0.3$ and 0.8 , that respectively cross the U_{c_2} and the U_{c_3} lines.

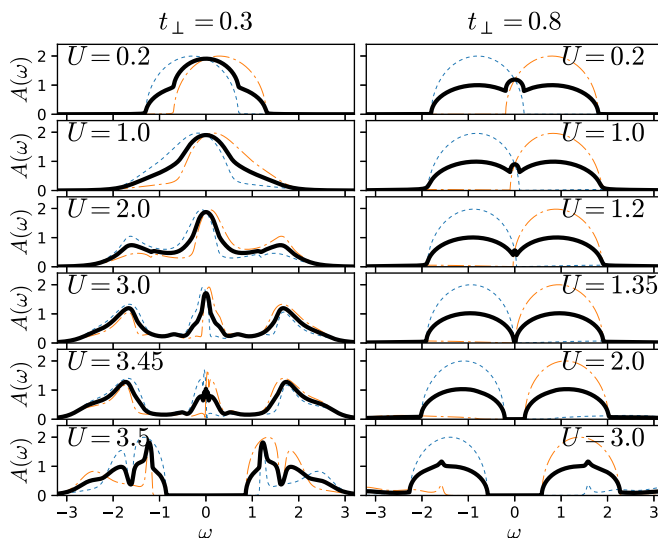


FIG. 4. DOS for increasing values of U crossing the red U_{c_1} and the green U_{c_3} boundary lines (left and right panels, respectively) of the phase diagram of Fig. 3. Black lines represent the local $(-\text{Im}G_{11})$ spectral function, which is the average of the bonding (dashed blue) and antibonding (dotted-dashed orange) bands, calculated at $T = 0$ with IPT.

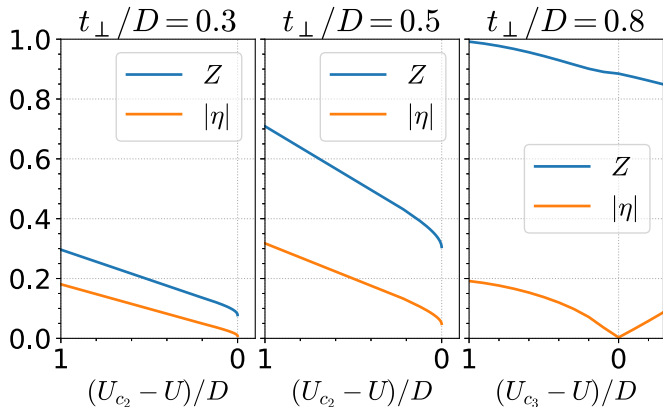


FIG. 5. Z and $|\eta|$ as a function of U for various values of dimerization t_{\perp} . The left and central panels correspond to the behavior as the $U_{c_2}(t_{\perp})$ red spinodal line is approached (cf. Fig. 3), where the metal-insulator transition is discontinuous. The right panel shows the behavior when the green second-order line is crossed (cf. Fig. 3). The R2B parametrization works on either side of the transition. Note that η is negative on the insulating side in the last panel.

The behavior of the DOS at higher $t_{\perp} = 0.8$ displays a rather simple evolution. As shown by the data in the B/AB basis (dotted blue and dotted-dashed orange) we observe that the total DOS (thick black) is the average of the two semicircular contributions of the B and AB bands. The gap opens continuously and the effective masses or, equivalently, the bandwidth of the two bands remains essentially unrenormalized. The insulator at $U > U_{c_3}$ is clearly a band insulator state. As we mentioned before, we identify this state with the Peierls insulator since it is realized at large t_{\perp} and relatively low U . We may also note that at the highest values of the interaction U , this simple description begins to fail as the B and AB DOS begin to develop a second contribution to the spectral weight for $\omega > 0$ and < 0 , respectively. We shall discuss this feature in more detail later on.

In contrast, the transition at lower values of $t_{\perp} = 0.3$ is significantly different. The evolution of the DOS is more complex and has various contributions. We can immediately observe the strongly correlated (Mott-Hubbard) character by noticing a characteristic three-peak structure at intermediate values of the interaction. The central peak, which gives the metallic character, becomes narrower as it loses spectral weight that is transferred to build the high-energy Hubbard bands at energy of order $\pm U/2$. Interestingly and contrary to the single-band Hubbard model case, there is no pinning condition for the central quasiparticle peak [27] and this quasiparticle develops a nontrivial structure in the DOS at low frequencies as the critical value U_{c_2} is approached. We shall come back to this point also later on. Unlike the higher- t_{\perp} case, the decomposition of the DOS in the B/AB contributions does not seem to provide any simpler picture of the evolution.

We can gain further insight on this transition by tracking the behavior of the self-energy through the two parameters that we defined above for the R2B model, Z and η , that we show in Fig. 5.

Consistent with our previous discussion, in the $t_{\perp} = 0.8$ case we see the parameter $|\eta|$ continuously and linearly going

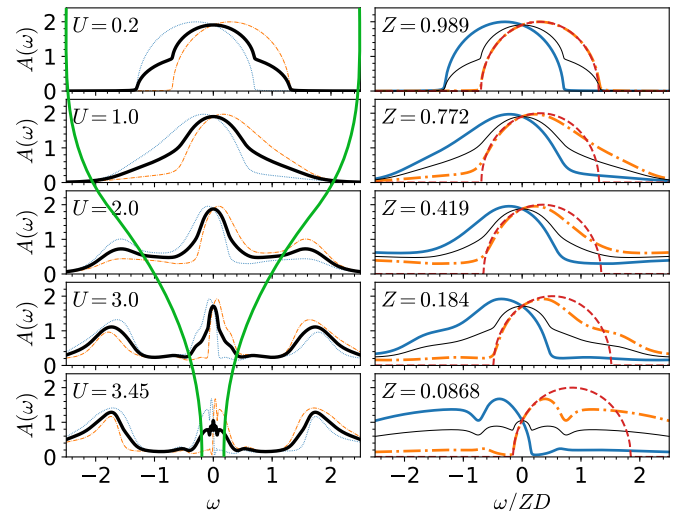


FIG. 6. Low-frequency scaling of the metallic DOS from Fig. 4 for increasing U at fixed $t_{\perp} = 0.3$. Right panels show a zoom into the corresponding low-frequency region that is indicated with green lines in the left panels. The local spectral function (black lines) is decomposed in the bonding spectral function (blue line) and antibonding spectral function (orange dotted-dashed line). The dashed red line is the renormalized parametrization of the low-energy quasiparticle from Eq. (6). The superposition of the two bands decreases as the system approaches the critical value $U_{c_2} \approx 3.47$. The size of the superposition is the vanishing scale η , which in this scaled plot is $\eta/ZD = 1 - \tilde{t}_{\perp}/D$.

to zero at both sides of the transition ($\eta > 0$ in the metal). The parameter Z remains close to one, which indicates an almost negligible mass enhancement. As one lowers the value of t_{\perp} to 0.5, we observe that the Z parameter begins to experience a bigger renormalization. Further down, for $t_{\perp} = 0.3$ the mass renormalization ($\propto 1/Z$) is very large. Thus, the metal state is strongly correlated with heavy quasiparticles. We can think of such a state at low energies as resulting from two “Kondo” states at each one of the atomic impurity sites. Each one of the sites is independently screened by conduction electrons, and also by each other. This leads to renormalized bonding and antibonding heavy bands as was already discussed in our previous paper [14]. Here, we shall be concerned with the question of how this heavy metallic state breaks down as U is increased.

A heavy metal with a (single) band and divergent mass is a hallmark of the metal-insulator transition in the single-band Hubbard model within DMFT [26]. That transition is a realization of the well-known Brinkman-Rice scenario, where the effective mass diverges at the metal-insulator transition. In the present dimer model, we shall see that, despite a large renormalization of the effective mass, it does not diverge and the transition is qualitatively different.

Motivated by the previous discussion and by Eqs. (5) and (6) of the renormalized two-band model, we close up on the low-frequency peak of the spectra of Fig. 4 and we replot the DOS in Fig. 6 as a function of the rescaled frequency ω/ZD . We see that a clear picture emerges, where the central peak can be understood as two bands whose splitting is renormalized down but whose width is also renormalized down. The R2B model

parametrization (in dashed red line in the figure) provides a good representation of the lowest-frequency part of the spectra, made by the low-energy edges of the B and AB peaks. Otherwise, it is not very accurate.

Unlike in the Brinkman-Rice scenario, where $Z \rightarrow 0$, here the transition occurs at a finite effective mass. The opening of the gap results from the combined effect of the renormalization of the bandwidth and of the splitting. Both decrease as $U \rightarrow U_{c_2}(t_\perp)$, but the quantity that becomes zero is not Z but the renormalized B/AB band overlap $\eta = ZD - Z\tilde{t}_\perp$. This means that the low-energy B and AB contributions to the quasiparticle peak separate. This behavior is similar to the MIT reported in a correlated two-orbital model [33]. Despite the lack of a mass divergence, the transition does share a similarity with the MIT in the single-band case, namely, that as the $\text{DOS}(\omega = 0)$ becomes zero, the Kondo effect can no longer be sustained and the impurities lose their respective Kondo screening clouds. In the single-band (single-site) case, in the Mott-insulator state one is left with almost free local moments. However, in the present situation, a strong RKKY-type magnetic interaction between the two sites takes over and one has intradimer magnetic screening. This dramatic enhancement of the intradimer magnetic interaction translates into the sharp increase of the intradimer effective hopping $\tilde{t}_\perp = t_\perp + \text{Re}\Sigma_{12}(0)$, which drives the opening of the gap (see Fig. 4) [14]. Interestingly, this sharp increase of the $\text{Re}\Sigma_{12}(0)$ was also observed in DFT+CDMFT calculations in VO_2 by Brito *et al.* [10]. They related this effect to the gap opening by the B/AB band splitting of the a_{1g} orbital in VO_2 . It is interesting to see that our present model Hamiltonian does capture the same basic physical mechanism, albeit in a simplified scenario that makes its physical interpretation transparent. Thus, we see how the renormalization of the intradimer hopping that drives the MIT originates in the loss of lattice Kondo screening and the concomitant boost of the local intradimer magnetic interaction. These competing mechanisms are well known in strongly correlated systems tracing back to Doniach's Kondo lattice [34]. Not surprisingly, the R2B model is unable to provide a proper description of the system beyond the transition in the Mott-insulator state (see Fig. 4). We shall come back to this point later on.

We should mention here that, within the IPT approximation and our numerical precision, η does not seem to vanish completely at intermediate values of t_\perp (≈ 0.5) as clearly as it does for smaller and larger values (see Fig. 5). We have also used CT-QMC at the lowest possible temperatures, but the results were inconclusive due to the very small energy scale being in competition with the low temperature. This issue might be eventually fully resolved by better adapted methods such as NRG-DMFT [35] or DMRG-DMFT [36].

B. Insulator-to-metal transition across U_{c_1}

An interesting feature of the solution of the DHM is the existence of a first-order transition driven by temperature [14]. This transition emerges as a consequence of two coexistent solutions found in a region of the phase diagram of the model [27] as we show in Fig. 7.

We have described above how the metallic solution collapses discontinuously as one increases the interaction U .

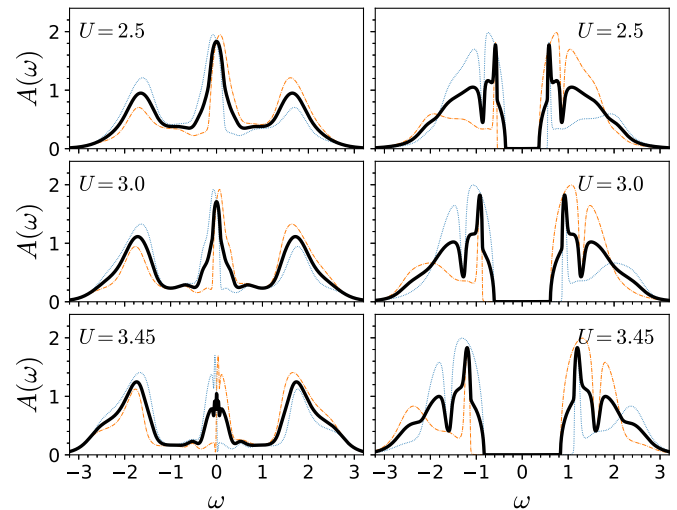


FIG. 7. DOS for increasing values of U and $t_\perp = 0.3$ within the coexistence region. Metallic solutions are shown on left panels and insulating ones on the right. Black lines represent the local $(-\text{Im}G_{11})$ spectral function, which is the average of the bonding (dashed blue) and antibonding (dotted-dashed orange) bands, calculated at $T = 0$ with IPT.

Here, we shall consider the collapse of the insulator one as we come down from high U towards U_{c_1} . The systematic behavior of the DOS is shown in Fig. 8 for two representative values of t_\perp : a smaller value $t_\perp = 0.4$ where the system crosses the U_{c_1} line and, for comparison, a larger value $t_\perp = 0.6$ which is closer to the continuous transition line U_{c_3} .

At the lower value of t_\perp we observe that the DOS does not seem to close the gap at the transition. Notice the choice

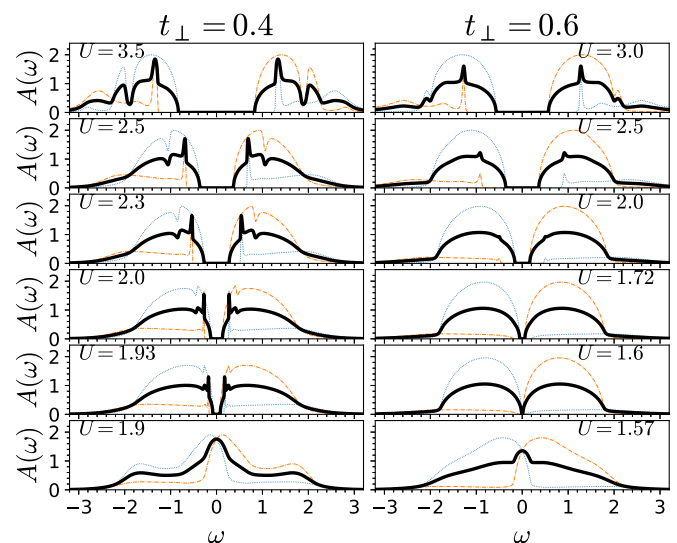


FIG. 8. DOS for decreasing values of U as the system crosses the U_{c_1} transition line (blue line of Fig. 3). Left panel is away from the tricritical point and right panel data are close to it. Black lines represent the local $(-\text{Im}G_{11})$ spectral function, which is the average of the bonding (dashed blue) and antibonding (dotted-dashed orange) bands, calculated at $T = 0$ with IPT. Note the discontinuous behavior as U_{c_1} is crossed.

of values of U very close to the critical point. The transition is clearly discontinuous since just below U_{c1} for $U = 1.9$ the DOS changes abruptly, displaying a metallic state that has a large quasiparticle peak. The line shape of the Hubbard bands is quite peculiar and we shall consider that feature later on. At the larger value of t_{\perp} , the system is still crossing the U_{c1} line. However, and in contrast to the previous case and within our numerical precision, the gap seems to close continuously. Nevertheless, and different to the behavior across the U_{c3} line that we described before (cf. Fig. 4), the character of the transition from insulator to metal remains discontinuous in regard of the DOS line shape. Indeed, as the results show, it changes quite significantly with only a tiny variation of U (lower two panels on the right-hand side of Fig. 8). Also, in contrast to the lower- t_{\perp} case, we see that the line shape of the DOS in the insulator has significantly less structure. This is due to the proximity of the parameters to those of the continuous transition, therefore, the first-order character becomes weaker as one approaches the *tricritical* transition point where the U_{c1} , U_{c2} , and U_{c3} lines meet.

IV. MOTT-PEIERLS INSULATOR-INSULATOR CROSSOVER

We now turn to the central part of our study, namely, the characterization of the multiple crossovers regimes in the DHM.

As we discussed already in the Introduction, the physical characterization of the VO_2 as Mott, Peierls, or “in-between” has been a tricky issue. As we shall see in this section, this can be explained by the rich physics and subtle behavior changes that the DHM exhibits as it crosses over from pure Mott to pure Peierls. We may define the former with respect to the prototypical Mott insulator that is realized in the one-band Hubbard model. As we already discussed in Sec. II, the DHM in the $t_{\perp} = 0$ limit becomes in fact two independent copies of the single-band Hubbard model. In such a regime, the electrons become localized because of the strong onsite Coulomb repulsion. This creates “free local moments” at every site, and the electronic structure is, accordingly, very *incoherent Hubbard bands* split by a large energy scale $\sim U$ [26]. The other extreme case, the pure Peierls, is identified in the DHM as the $U = 0$ limit with the B/AB bands having a $2t_{\perp}$ split, larger than the bandwidth $2D$. Hence, a gap in the DOS spectra opens by virtue of the momentum-independent strong dimerization hopping amplitude. This is a pure “band-structure” effect as the interaction U is set to zero. In this insulator state, the bonding and antibonding bands are separated and the former is fully filled with two electrons per dimer site. The system is a “band insulator,” which is nonmagnetic, and its electronic structure shows two parallel *coherent Bloch bands*. We shall explore in this section how the system transmutes from one regime to the other.

In Fig. 9 we show the various regimes that the system exhibits as it crosses over from the Mott to the Peierls limit. There are four different zones, which can be well characterized. The understanding of zone I is key to this study. Its important feature is an interesting *thermal* crossover where spin degrees of freedom are active. These magnetic moments are due to the Coulomb interaction and emerge as the result of Mott

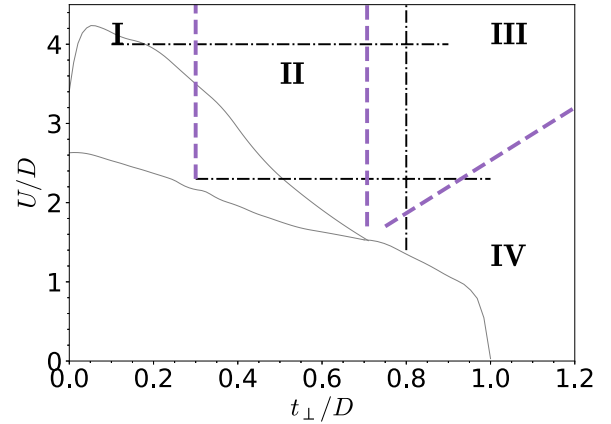


FIG. 9. The phase diagram of the model with the various crossover regimes I–IV that are described in the text. The dashed lines separating the different zones are for reference only since the evolution is continuous. The dashed-dotted lines denote the various paths across the diagram whose evolution we describe in the text. For reference, we draw as gray lines the U_{c1} , U_{c2} , and U_{c3} transitions (cf. Fig. 3).

localization above the U_{c1} line at low t_{\perp} . Zone IV is characterized by the insulating Peierls state. As we shall see, we can think of that state as “orbitally polarized” in the B/AB basis, with correlations playing a relatively minor role. The zones II and III have a mix character and the evolution of the electronic structure is quite subtle. We have therefore explored the evolution of the system across the different zones by following the black lines that are indicated in Fig. 9. We consider two parallel lines at fixed values of U and varying t_{\perp} . The relatively smaller U line traces the systematic evolution from within the Mott coexistence region towards the Peierls one. At a larger value of U we shall see that the system remains within a Mott state even for relatively large values of t_{\perp} . The main feature in this case is an interesting evolution of the electronic structure, going from incoherent Hubbard bands (zone I) to coherent ones (zone III) and passing through a *mixed* state with the coexistence of coherent and incoherent contributions (zone II). We shall describe these various crossovers in detail in the following subsections.

A. Zone I: Singlet to free-moment crossover in the Mott state

This regime at $U > U_{c1}$ and small t_{\perp} is crucial to understand the physical behavior of the present model. The large value of the onsite Coulomb repulsion U creates a local magnetic moment at each site of the dimer. Then, the interaction between these moments undergoes a *thermal crossover* from a singlet ground state at $T \rightarrow 0$ to a free-moment regime above a low-temperature scale T^* . This temperature is a low-energy scale of the model, which indicates the singlet pair formation and is two orders of magnitude smaller than the bare parameters. In Fig. 10 we show the behavior of the total magnetic moment formation $\langle (N_{\uparrow} - N_{\downarrow})^2 \rangle = \langle [(n_{1\uparrow} - n_{1\downarrow}) + (n_{2\uparrow} - n_{2\downarrow})]^2 \rangle$ as a function of t_{\perp} at different fixed temperatures. At any given temperature, we observe that the moment formation goes from a very small value at large t_{\perp} and suddenly has a dramatic increase upon lowering that parameter. The reason is that the

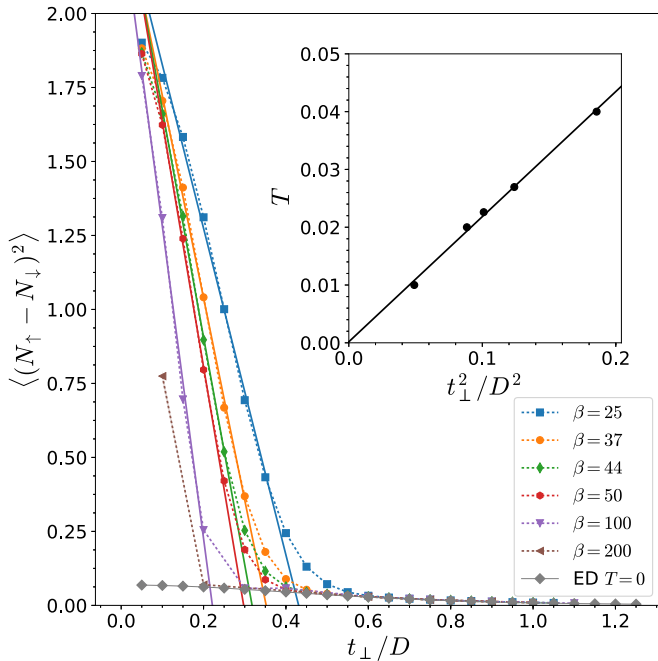


FIG. 10. Total magnetic moment formation as a function of t_{\perp} at different temperatures. Finite-temperature calculation done with CTHYB, and zero temperature with ED. Inset: temperature crossover scale for singlet pairing of the two site moments T^* . This scale is proportional to the square of t_{\perp} consistent with its magnetic origin.

magnetic coupling between the local moments at the two sites of the dimer is large at bigger t_{\perp} so they lock into a singlet state which is nonmagnetic. When this magnetic interaction is reduced by decreasing t_{\perp} , the magnetic binding energy falls below the thermal energy and the singlet state breaks down. The two local moments unbind and behave as local free spins analogous to the Mott-insulator state of the single-band Hubbard model.

This behavior can also be clearly seen by its dramatic effect on the electronic structure. In Fig. 11 we show in a color intensity plot the *bonding* spectral function dispersion $A_B(\epsilon, \omega)$ for the system at a fixed T and two values of t_{\perp} . One larger

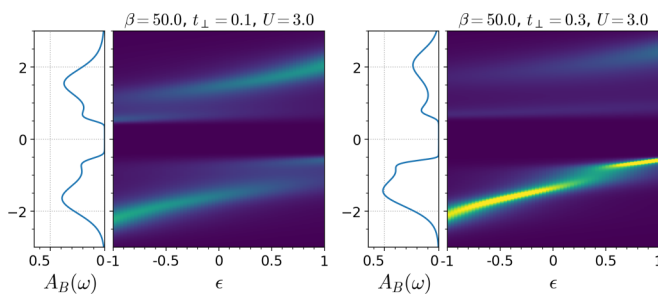


FIG. 11. Intensity plot of the *bonding* spectral function $A_B(\epsilon, \omega)$ at $U = 3$ and $t_{\perp} = 0.1$ and 0.3 calculated at $T = 0.02$, using CTHYB. In side panels we show the corresponding DOS(ω), i.e., the integrated *bonding* spectral function. We recall that in the Bethe lattice the single-particle energy plays an analogous role as the lattice momentum k . The noninteracting dispersion is $\epsilon - t_{\perp}$, with $-D < \epsilon < D$.

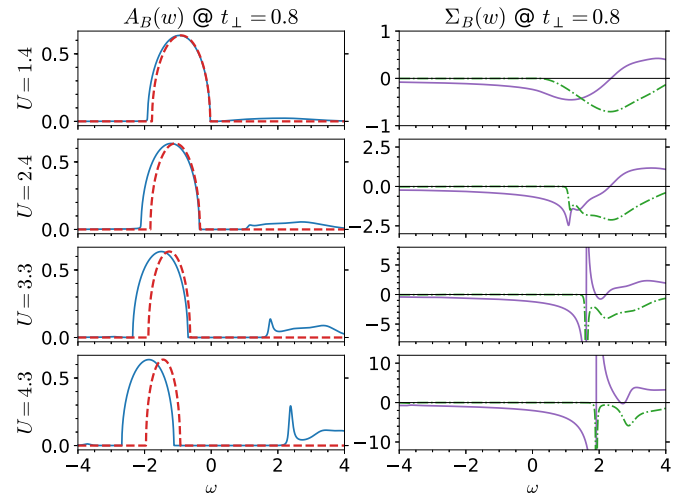


FIG. 12. Evolution of the bonding DOS(ω) and corresponding change in the bonding self-energy at fixed $t_{\perp} = 0.8$ (real part in solid lines and imaginary part in dotted-dashed lines) for increasing U . The location of this crossover path is indicated by one of the black dashed-dotted lines in Fig. 9. Red dashed lines correspond to the R2B model parametrization, which fails at large U .

$t_{\perp} = 0.3$ with the two moments locked into the singlet and a smaller one $t_{\perp} = 0.1$ with two unbound free moments.

The change in the spectral function is very significant and consistent with the magnetic state. To make the effect more explicit, we focus on the bonding spectral function. We recall that the antibonding is obtained by reflection around $\omega = 0$, and the site-basis one is the average of the two. At the higher value of t_{\perp} , the spectra are not symmetric; we see that the low-energy band has most of the spectral weight. This signals that the system is locked in the singlet bound state, with the bonding band almost fully occupied. In contrast, at lower t_{\perp} the state is not magnetically bound and correspondingly we obtain a symmetric spectrum. The AB state is virtually identical to the B one, so both have a similar occupation, which indicates that the magnetic states are decoupled and free to fluctuate as in the Mott insulator in the single-band case. In fact, the spectral function of the low- t_{\perp} case that is above T^* is very similar to the incoherent Hubbard bands of the single-band Mott-Hubbard insulator [26], which is nothing but the $t_{\perp} = 0$ case.

This physical insight is a key reference to guide the discussion of the various t_{\perp} - and U -dependent crossovers that we shall describe next. In fact, we shall see that the emerging magnetic moments, characteristic of the Mott localization phenomenon, will show up in different contributions to the electronic structure.

B. Zone IV-III and IV-I crossovers: Building correlations on the Peierls state

We have just discussed how the local moment degrees of freedom that are present in zone I due to Mott localization may bind or unbind. Now, we will discuss how in the Peierls nonmagnetic state (large t_{\perp} and $U = 0$), the magnetic moments gradually emerge as the correlations are increased. To illustrate that, we plot in Fig. 12 the evolution of the bonding orbital DOS, i.e., the $A_B(\omega)$ spectral function for increasing U , along

with its corresponding self-energy $\Sigma_B(\omega)$. At weak correlations, for $t_\perp = 0.8$ and $U = 1.4$, the system is still within the Peierls insulating state in zone IV. We observe that the R2B model parametrization (red dashed line) provides a rather good description. The occupation of the B state is almost complete, so we may consider this state as fully orbitally polarized in the B/AB basis. Accordingly, the self-energy remains smooth and small.

Increasing U , the system crosses over from zone IV to III and we observe qualitative changes in both the DOS and Σ . For $U = 2.4$ we already see an incipiently structured spectral weight developing at $\omega > 0$. Accordingly, the self-energy begins to develop a rapidly varying wiggle. These developing structures become apparent at a higher interaction strength $U = 3.3$. We clearly observe the emergence of a quasiparticle-like resonance in the DOS, with a concomitant pole in the self-energy. This signals the onset of a well-defined excitation and the narrowness of the peak indicates that it is essentially a localized state. This excitation is in fact due to local moments building up at each of the dimer sites [14]. Unlike in the Mott state at low t_\perp , where the local moments produce a broad incoherent contribution to the spectral function, here the moments are strongly coupled by the large t_\perp . Therefore, they remain Mott localized *within* the dimer but establish a local coherent (singlet) state. Upon further increasing the interaction U , the resonance gains more spectral weight and the strength of the pole also grows. The ‘‘Mottness’’ character of the state increases as we see that the simple renormalized two-band

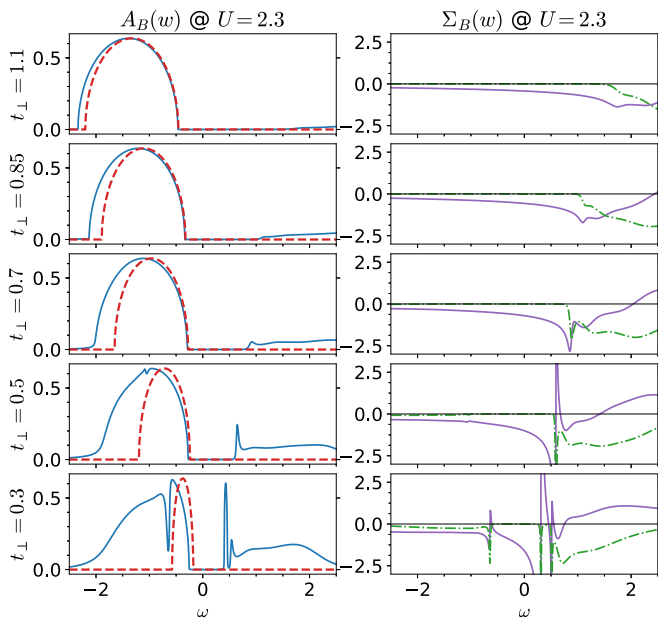


FIG. 13. Evolution of the bonding DOS(ω) and corresponding change in the bonding self-energy (real part in solid lines and imaginary part in dotted-dashed lines) at fixed $U = 2.3$ for decreasing t_\perp . The location of this crossover path is indicated by one of the black dashed-dotted lines in Fig. 9. Red dashed lines correspond to the R2B model parametrization, which fails at lowest t_\perp . While there is a sharp narrow peak at the $\omega > 0$ of the spectra (lower panel), we are not fully confident in the presence of the small secondary peak being a separate excitation.

parametrization fully breaks down. Notice, however, that in contrast to the pure Mott insulator with incoherent Hubbard bands, here the lower Hubbard band in $A_B(\omega)$ remains fully coherent as in the Peierls insulator case. This is evident from the imaginary part of the self-energy (bottom right panel of Fig. 12), which is negligible on the full $\omega < 0$ frequency range. We thus begin to observe the coexistence of incoherent and coherent features in the electronic structure, which are respectively connected to Mott and Peierls physics.

We now turn to the crossover behavior from zone IV to zone I (cf. Fig. 9). The systematic behavior is shown for $A_B(\omega)$ and $\Sigma_B(\omega)$ in Fig. 13. We observe that all the features that we described before in the zone IV to III crossover as a function of U are also present here as the system evolves as a function of the model parameter t_\perp . It crosses over from the Peierls insulator in zone IV towards the Mott state in zone I. Similarly as before, we observe the emergence of a narrow resonance in the $\omega > 0$ part of the spectra. However, a difference with the previous crossover is that the evolution now ends close to the pure Mott state and we see that the $\Sigma_B(\omega)$ is non-negligible at $\omega < 0$. One may notice that this second crossover path traverses the zone II. The clear characterization of that regime requires the discussion of the spectral function $A(\epsilon, \omega)$, which we shall consider in the next subsection.

V. EVOLUTION OF THE DIMER MOTT INSULATOR: COEXISTENT INCOHERENT AND COHERENT CONTRIBUTIONS

We now finally consider the strongly correlated regime set by a relatively large value of the interaction $U = 4$. We shall discuss the systematic changes of the insulator state as

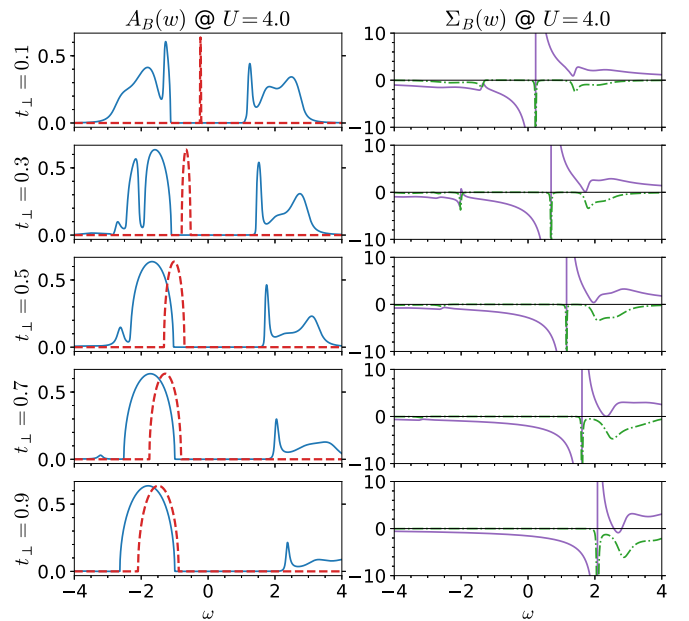


FIG. 14. Evolution of the bonding DOS(ω) and corresponding change in the bonding self-energy (real part in solid lines and imaginary part in dotted-dashed lines) at fixed $U = 4$ for increasing t_\perp . The location of this crossover path is indicated by one of the black dashed-dotted lines in Fig. 9. Red dashed lines correspond to the R2B model parametrization, which is always poor in this case.

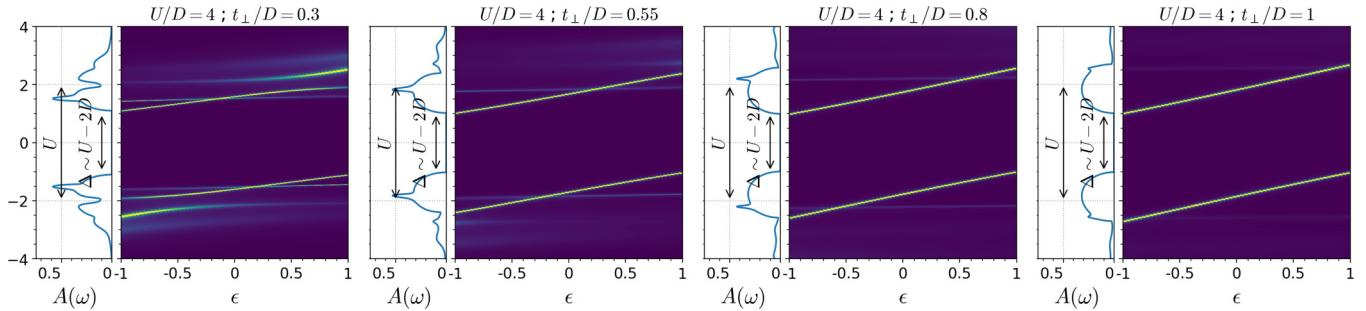


FIG. 15. Local density of states $A(\omega)$ (vertical panels) and intensity plots of the spectral function $A(\epsilon, \omega)$ of the Mott-insulating state at large $U = 4$ and increasing t_{\perp} . Obtained by IPT at $T = 0$.

it evolves as a function of increasing intradimer hopping t_{\perp} . As we did before, we begin considering the bonding DOS $A_B(\omega)$ and the corresponding self-energy $\Sigma_B(\omega)$, which unveils details of its mathematical structure. The data are shown in Fig. 14. We recall that the same quantities on the AB orbital are obtained by reflection around $\omega = 0$, and that the total DOS corresponds to the average of the B and AB. The main feature is that there is always a large gap with two main contributions at $\omega \sim \pm U/2$. Thus, for all t_{\perp} we have a large insulating gap controlled by U , which is an indication of Mott physics having a dominant role. We also see, consistent with this observation and with our discussion in previous sections, that the unoccupied part of $A_B(\omega)$ always has a sharp resonance that we associated to emergent magnetic moments. Moreover, in $\Sigma_B(\omega)$ we always observe the presence of a strong pole. Interestingly, we see that the position of the pole is almost at the center of the gap at lower t_{\perp} . In fact, it must reach $\omega = 0$ in the limit of $t_{\perp} \rightarrow 0$ as system the becomes two independent copies of a single-band Mott insulator [26]. Thus, this strong pole is a hallmark of the opening of a Mott gap. As we increase t_{\perp} we see that the pole remains strong but evolves towards the upper edge of the gap. This has the effect of strongly affecting the $\omega > 0$ part of the spectrum while we observe that the $\omega < 0$, in contrast, evolves towards the semicircular density of states. This apparent weakening of correlations in the lower Hubbard band can be also understood by the fact that this band is further filled up, hence effectively moving away from the half-filled situation. However, it would be a mistake to simply consider this a weakly correlated state since, as we already emphasized, the gap is large and set by the Coulomb interaction U . In fact,

we observe that the R2B model parametrization (red dashed line in Fig. 14) is poor in all cases.

Another interesting feature revealed by the $\Sigma_B(\omega)$ is that the imaginary part, which is related to the inverse lifetime, is always relatively large on the $\omega > 0$ side of the spectra while is much smaller, or even negligible, for larger t_{\perp} on the $\omega < 0$ side. This indicates that the positive frequency excitations have incoherent character (save for the sharp resonance state that we discussed in previous sections), while the negative frequency ones are coherent. One additional interesting feature that we would like to point out is the complex evolution of the line shape of $A_B(\omega)$ at small t_{\perp} , where $\text{Im}\Sigma_B$ is still non-negligible. This regime corresponds to the crossover zone II (cf. Fig. 9). In order to gain further insight into these issues, we shall consider the “momentum” resolved spectral function $A(\epsilon, \omega)$ along with the local DOS, $A(\omega) = \int d\epsilon A(\epsilon, \omega)$.

For the sake of clarity, we consider both the total (i.e., site basis) and bonding orbital spectral functions. Their evolution is shown, respectively, in Figs. 15 and 16. We should actually begin with the spectra already shown in Fig. 11, which illustrated the very low- t_{\perp} regime (zone I) where the system is deep in the Mott phase with decoupled magnetic moments (at finite $T > T^*$). Consequently, the $A(\epsilon, \omega)$ displays a very incoherent electronic structure, similar to the single-band Mott state.

As we increase the t_{\perp} in Figs. 15 and 16 we observe the systematic evolution of the electronic structure. It always shows two roughly parallel lower and upper Hubbard bands split by U . These bands gain in coherence as t_{\perp} is increased. At the end state, i.e., higher t_{\perp} , two well-defined and coherent

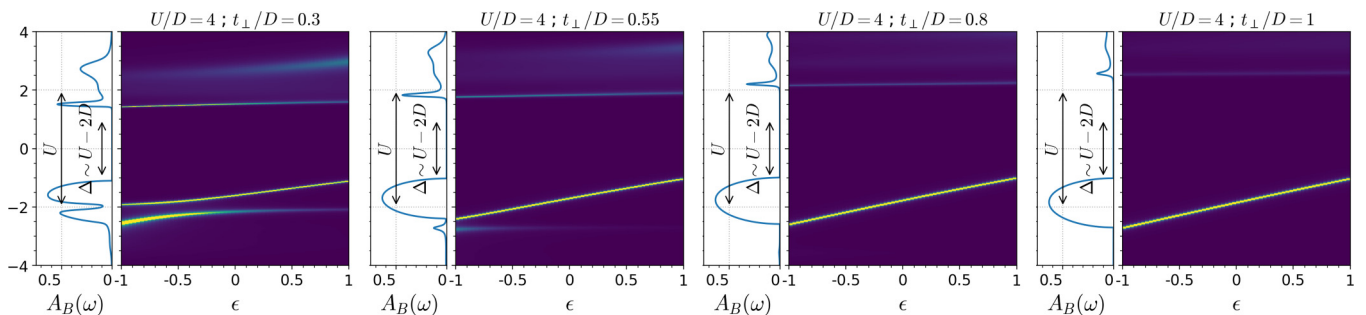


FIG. 16. Bonding density of states $A_B(\omega)$ (vertical panels) and intensity plots of the bonding spectral function $A_B(\epsilon, \omega)$ of the Mott-insulating state at large $U = 4$ and increasing t_{\perp} . Obtained by IPT at $T = 0$. Note these are the same data as in Fig. 15 but shown on a different basis.

contributions dominate the electronic structure. As can be seen in the last panel of Fig. 16, the main contribution comes from the bonding state for the lower Hubbard band, and correspondingly from the antibonding for the upper Hubbard one. However, some incoherent weak intensity and weakly dispersive states can still be observed. This state resembles the Hubbard I solution, with two coherent bands, that are split by U . This can be rationalized noting that in the B/AB basis, the system is strongly orbitally polarized.

More interesting are the states at lower values of t_{\perp} . As displayed in the first two panels of Fig. 16, we observe that the Hubbard bands develop a unique characteristic, which is their mixed character. In fact, we observe sharper and more coherent quasiparticlelike contributions to the electronic structure in the inner edges of the Hubbard bands, which upon integration lead to a peculiar line shape for the local DOS(ω). The outer part of the Hubbard bands, in contrast, is strongly incoherent. The physical interpretation of the quasiparticle states stems from the intradimer magnetic coupling of the emergent moments. Within the dimer they develop a coherent singlet state, thus remain localized, and their effective mass is heavy. The propagation of higher-energy states through the lattice remains very incoherent, as signaled by the diffuse spectral intensity which is broad on a scale of $\sim D$. These states with a mixed character in the propagation of the Hubbard bands are an original feature of the DHM and they are absent in the single-band model case. It would be interesting to see if some of its signatures may be experimentally observed in spectroscopic studies.

VI. CONCLUSIONS

We have studied in detail the solution of a basic strongly correlated model, the dimer Hubbard model, which is possibly relevant for VO₂ [14], monoclinic transition-metal oxides MO₂ [25], and more generally structures with a dominating bond between a pair of correlated metallic ions.

This model is also interesting as it is arguably the simplest realization of a cluster DMFT problem and has a quantum impurity model that is analogous to that of realistic DFT+DMFT calculations of monoclinic VO₂. Indeed, we have seen that the solution of the DHM does exhibit the same physical mechanism for the insulator gap opening as was reported in DFT+DMFT studies, namely, the strong enhancement of the intradimer self-energy.

We provided a detailed description of the solutions in the “coexistent region” where two (meta)stable states of the CDMFT equations are found: one a metal and the other an insulator. Moreover, we described in detail how these states break down at their respective critical lines. We have clarified the key role played by the intradimer correlation, which here acts in addition to the familiar onsite Coulomb correlations (Mott-Hubbard) that were already present in the one-band case. Their interplay (i.e., Kondo screening vs RKKY) determines the physics of the metal-to-insulator transition line as the instance where the renormalized low-energy B/AB bands separate. This was described in terms of our R2B model parametrization, which turned out to be always applicable in metallic side on the full $t_{\perp} - U$ phase diagram at low enough frequencies, but not in the Mott-insulator state.

The simplicity of the DHM provides new and detailed physical insight and allows us to clarify the important issue of the Mott-Peierls crossover. This question has remained a matter of debate in DFT+CDMFT studies for VO₂. A reason may be found in the surprisingly subtle evolution of the electronic structure with the systematic change of model parameters. In fact, the crossover from the Mott to the Peierls limit is nontrivial and we characterized a variety of physical regimes. Interestingly, we found that the Hubbard bands evolve from purely incoherent (Mott) to purely coherent (Peierls) through a state with unexpected mixed character. This feature can be understood as follows: in the Mott limit, at low intradimer hopping t_{\perp} , one has emergent magnetic degrees of freedom that remain freely fluctuating above a rather small spin-singlet pairing temperature T^* . Increasing the intradimer hopping, the moments bind into a spin-singlet state and they acquire coherence (i.e., a well-defined quantum state) within the dimer. However, the excitations of such a state still lack coherence through the lattice. We may think of this state as Mott-localized singlet dimers. Upon further increase of the intradimer hopping, the bonding orbital becomes fully occupied as one may think of t_{\perp} as an effective crystal field. Hence, the system becomes orbitally polarized in the bonding/antibonding basis, which renders the electronic structure coherent as quantum fluctuations are frozen out. Nevertheless, even in this large- t_{\perp} limit, the gap remains controlled by the interaction U . Therefore, the state remains a Mott-insulator one at strong enough U (zone III on Fig. 9), and although it is in a B/AB polarized state, it can be seen that a Hartree-Fock description fails.

Our work has uncovered a paradigm of a nonmagnetic Mott insulator, which may be realized in structures with two strongly coupled correlated atoms, with VO₂ as a prototypical example. This Mott state has a surprising coexistence of coherent and incoherent excitations. An open question is whether this feature may be seen in spectroscopic studies, or if it may be put in evidence by pump-probe experiments that may selectively excite particles to the coherent or incoherent states.

Finally, the intradimer magnetic coupling provides binding of the two electrons into a singlet state below a characteristic temperature T^* . It is an interesting open question to study the fate of such a state upon doping the system. This situation is rather reminiscent of the magnetic pseudogap state discussed in the context of the doped Mott state of cuprate superconductors.

APPENDIX A: DETAILS OF THE TWO-RENORMALIZED-BAND APPROXIMATION AT LOW FREQUENCIES

In order to derive a simple description of the low-frequency electronic structure in a large region of parameter space, it is useful to expand the mean-field equations (2) at low energies $\omega \rightarrow 0$ once they are in diagonal form:

$$G_{B/AB}(\omega) = \int d\varepsilon \rho(\varepsilon) [\omega - \varepsilon \pm t_{\perp} - \Sigma_{B/AB}(\omega)]^{-1}. \quad (\text{A1})$$

From this equation, one approximates the self-energy assuming it has a well-behaved Taylor expansion up to linear order in the interval $0 < \omega < \omega^*$, i.e., $\text{Re}\Sigma_{B/AB}(0) \approx \text{Re}\Sigma_{B/AB}(\omega^*)$, we can

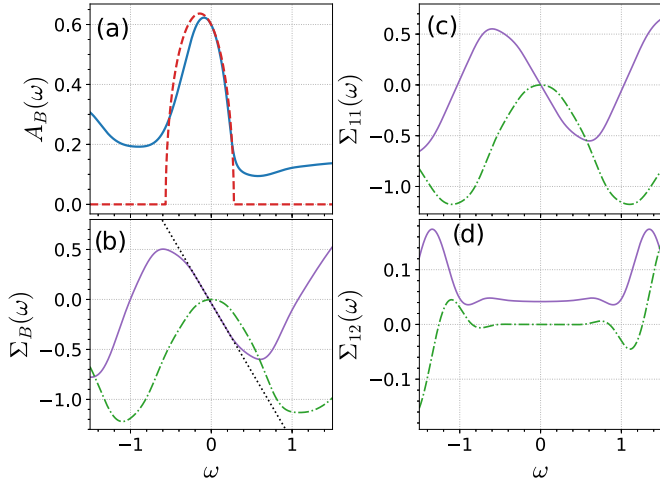


FIG. 17. Low-energy behavior of the spectral function and self-energy for the dimer system in the metallic phase at $t_{\perp}/D = 0.3$ $U/D = 2$. (a) Bonding spectral function $A_B(\omega)$ in orange and bonding renormalized band in dashed red lines providing a good agreement with the band edge of the spectral function. (b) The corresponding self-energy in the bonding basis Σ_B . In the site basis, (c) the same site Σ_{11} and (d) intersite Σ_{12} self-energies. Solid lines are the real parts and in dotted-dashed lines the imaginary parts. As expected in the quasiparticle regime $\text{Im}\Sigma \approx 0$ and the real part is linear.

write

$$\Sigma_{B/AB}(\omega) \approx \Sigma_{B/AB}(\omega = 0) + \left. \frac{\partial \Sigma_{B/AB}(\omega)}{\partial \omega} \right|_{\omega=0} \omega \quad (\text{A2})$$

and call this the quasiparticle interval where this approximation holds. The quasiparticles are long lived provided $\text{Im}\Sigma_{B/AB}(\omega) \approx 0$. In such a way, we may then represent the low-energy Green's function as

$$G_{B/AB}^{\text{R2B}}(\omega) = \int d\varepsilon \rho(\varepsilon) \left[\omega \left(1 - \left. \frac{\partial \text{Re}\Sigma_{B/AB}(\omega)}{\partial \omega} \right|_0 \right) - \varepsilon \pm t_{\perp} - \text{Re}\Sigma_{B/AB}(0) \right]^{-1}, \quad (\text{A3})$$

defining as in the main text the quasiparticle residue Z by

$$Z^{-1} \equiv 1 - \left. \frac{\partial \text{Re}\Sigma_{B/AB}(\omega)}{\partial \omega} \right|_0 = 1 - \left. \frac{\partial \text{Re}\Sigma_{11}(\omega)}{\partial \omega} \right|_0 \quad (\text{A4})$$

and the renormalized intradimer hopping

$$\tilde{t}_{\perp} \equiv t_{\perp} \mp \text{Re}\Sigma_{B/AB}(0) = t_{\perp} + \text{Re}\Sigma_{12}(0), \quad (\text{A5})$$

where the last equivalences are due to $\text{Re}\Sigma_{11}(0) = 0$ and $\left. \frac{\partial \text{Re}\Sigma_{12}(\omega)}{\partial \omega} \right|_0 = 0$ as can be verified in Fig. 17. Thus, we obtain a renormalized two-band (R2B) representation of the electronic structure at low ω in terms of two quasiparticle bands. Their corresponding DOS is composed of two narrowed semicircles of width $2\tilde{D} = 2ZD$ and split by $2Z\tilde{t}_{\perp}$,

$$\rho_{B/AB}^{\text{R2B}}(\omega) = \frac{2}{\pi D^2} \sqrt{D^2 - \left(\frac{\omega}{Z} \pm \tilde{t}_{\perp} \right)^2}. \quad (\text{A6})$$

Under this approximation, the total spectral weight of this renormalized band is not one any more but $Z < 1$ and the rest

of the spectral function outside the quasiparticle regime has totally vanished. However, this renormalized two-band system is well capable of representing the low-energy states of the system, especially the band edges of the quasiparticle peaks through which we are able to quantify the metal-to-insulator transition, as described in the main text. This simple low-frequency description in terms of two bands is accurate enough in a large region of the phase diagram, where the $\text{Re}\Sigma_{B/AB}$ is well behaved as mentioned above. These regions include the weakly correlated limit but also the strongly correlated metal.

It is important to recognize that the quasiparticle residue Z defined in Eq. (A4) does not follow the standard definition of a Landau-Fermi quasiparticle. In such case one would first find quasiparticles by finding the poles $\omega^*(\varepsilon)$ of the spectral function given by the solution of the equation

$$\omega^* - \varepsilon \pm t_{\perp} - \text{Re}\Sigma_{B/AB}(\omega^*) = 0. \quad (\text{A7})$$

In that case, one finds the quasiparticle residue for each Landau quasiparticle at every instance of the spectral dispersion, for each of the composing bands of the system.

$$Z_{B/AB}^{\varepsilon} \equiv \left[1 - \left. \frac{\partial \text{Re}\Sigma_{B/AB}(\omega)}{\partial \omega} \right|_{\omega=\omega^*(\varepsilon)} \right]^{-1}. \quad (\text{A8})$$

This treatment is unnecessary for our current specific purposes since we are working with an energy-averaged spectral function and in our particle-hole symmetric half-filled case, the simple expansion around $\omega = 0$ provides an excellent description of the low-energy features of the spectral function, in particular the band edges, which we use to quantify the transition.

APPENDIX B: PROOF THAT THE IPT SOLUTION IS EXACT AT $T = 0$ FOR THE ISOLATED DIMER (ATOMIC LIMIT OF THE DHM)

At the heart of the dimer lattice problem is a hydrogen molecule motive (the dimer) which repeats in the lattice. Isolating this molecule in the limit $t \rightarrow 0$, the governing Hamiltonian is reduced to

$$H = t_{\perp} \sum_{\sigma} (c_{1\sigma}^{\dagger} c_{2\sigma} + c_{2\sigma}^{\dagger} c_{1\sigma}) + U(n_{1\uparrow} n_{1\downarrow} + n_{2\uparrow} n_{2\downarrow}) - \mu \sum_{\alpha, \sigma} n_{\alpha\sigma}, \quad (\text{B1})$$

where $c_{\alpha\sigma}$ annihilates an electron from the dimer orbital $\alpha = \{1, 2\}$ and with spin $\sigma = \{\uparrow, \downarrow\}$. $U > 0$ is the onsite repulsive Hubbard interaction and $t_{\perp} > 0$ the dimer hybridization. The chemical potential is fixed to ensure half-filling at $\mu = U/2$.

In this work, the fermionic arrangement convention is to order states by their spin projection. Thus, the full occupation is described by the many-body state vector

$$|1\uparrow 2\uparrow 1\downarrow 2\downarrow\rangle = c_{1\uparrow}^{\dagger} c_{2\uparrow}^{\dagger} c_{1\downarrow}^{\dagger} c_{2\downarrow}^{\dagger} |\emptyset\rangle. \quad (\text{B2})$$

The single-particle sector has only four states, as one has four particles. After diagonalizing this block, we only find two distinct energy levels since up and down spin are degenerate.

We call these two levels the bonding (B) and antibonding (AB) levels:

$$|B\sigma\rangle = \frac{1}{\sqrt{2}}(|1\sigma\rangle - |2\sigma\rangle), \quad E_B = -\frac{U}{2} - t_\perp, \quad (\text{B3a})$$

$$|AB\sigma\rangle = \frac{1}{\sqrt{2}}(|1\sigma\rangle + |2\sigma\rangle), \quad E_{AB} = -\frac{U}{2} + t_\perp. \quad (\text{B3b})$$

The ground state is in the $N = 2$ sector and it is nondegenerate $\forall U > 0$ and $\forall t_\perp > 0$. Its energy eigenvalue and eigenvector are

$$E_{\text{GS}} = -\frac{U}{2} - \frac{1}{2}\sqrt{U^2 + 16t_\perp^2}, \quad (\text{B4a})$$

$$|\text{GS}\rangle = \frac{1}{a} \left((|1\uparrow 2\downarrow\rangle + |2\uparrow 1\downarrow\rangle) - \frac{4t_\perp}{U+b} (|1\uparrow\downarrow\rangle + |2\uparrow\downarrow\rangle) \right), \quad (\text{B4b})$$

where $a = \sqrt{\frac{32t_\perp^2}{(U+b)^2} + 2}$ and $b = \sqrt{U^2 + 16t_\perp^2}$. It becomes clear from this that as the local Coulomb interaction is raised, the double occupation is reduced in the system. The zero-temperature Green's function of the dimer can be obtained through the Lehmann representation by

$$G_{\alpha\beta\sigma}(\omega) = \sum_m \frac{\langle \text{GS} | c_{\alpha\sigma} | m_{N=3} \rangle \langle m_{N=3} | c_{\beta\sigma}^\dagger | \text{GS} \rangle}{\omega - (E_m - E_{\text{GS}})} + \sum_m \frac{\langle m_{N=1} | c_{\alpha\sigma} | \text{GS} \rangle \langle \text{GS} | c_{\beta\sigma}^\dagger | m_{N=1} \rangle}{\omega - (E_{\text{GS}} - E_m)}, \quad (\text{B5})$$

which reduces for the local (G_{11}) and intersite (G_{12}) Green's functions into

$$G_{11\sigma} = \frac{1}{a^2} \left[\frac{(1 - \frac{4t_\perp}{U+b})^2}{a^2(b + 2t_\perp + 2\omega)} - \frac{(1 - \frac{4t_\perp}{U+b})^2}{a^2(b + 2t_\perp - 2\omega)} + \frac{(1 + \frac{4t_\perp}{U+b})^2}{a^2(b - 2t_\perp + 2\omega)} + \frac{(1 + \frac{4t_\perp}{U+b})^2}{a^2(-b + 2t_\perp + 2\omega)} \right], \quad (\text{B6a})$$

$$G_{12\sigma} = \frac{1}{a^2} \left[\frac{(1 - \frac{4t_\perp}{U+b})^2}{(b + 2t_\perp + 2\omega)} + \frac{(1 - \frac{4t_\perp}{U+b})^2}{(b + 2t_\perp - 2\omega)} - \frac{(1 + \frac{4t_\perp}{U+b})^2}{(b - 2t_\perp + 2\omega)} + \frac{(1 + \frac{4t_\perp}{U+b})^2}{(-b + 2t_\perp + 2\omega)} \right]. \quad (\text{B6b})$$

The self-energy is obtained by solving Dyson's equation, which is a matrix equation of the form

$$\begin{bmatrix} \Sigma_{11} & \Sigma_{12} \\ \Sigma_{12} & \Sigma_{11} \end{bmatrix} = \begin{bmatrix} \omega & -t_\perp \\ -t_\perp & \omega \end{bmatrix}^{-1} - \begin{bmatrix} G_{11} & G_{12} \\ G_{12} & G_{11} \end{bmatrix}^{-1} \quad (\text{B7})$$

and results in

$$\Sigma_{11} = \frac{U^2}{4} \frac{\omega}{\omega^2 - 9t_\perp^2} = \frac{U^2}{8} \left(\frac{1}{\omega + 3t_\perp} + \frac{1}{\omega - 3t_\perp} \right), \quad (\text{B8a})$$

$$\Sigma_{12} = \frac{U^2}{4} \frac{3t_\perp}{9t_\perp^2 - \omega^2} = \frac{U^2}{8} \left(\frac{1}{\omega + 3t_\perp} - \frac{1}{\omega - 3t_\perp} \right). \quad (\text{B8b})$$

The IPT scheme is drastically simplified in the isolated molecule case as it becomes a single iteration procedure. The self-energy is directly approximated by the second-order diagram

$$\Sigma_{\alpha\beta}(i\omega_n) \approx -U^2 \int_0^\beta G_{\alpha\beta}^0(\tau) G_{\alpha\beta}^0(-\tau) G_{\alpha\beta}^0(\tau) e^{i\omega_n \tau} d\tau. \quad (\text{B9})$$

In this case, one does not include the Hartree term as for the particle-hole symmetric case it is exactly canceled by the chemical potential. The IPT equation (B9) can be conveniently reformulated into real frequencies by the analytical continuation and we can focus only on the imaginary part only needing the spectral functions [37]:

$$\begin{aligned} \text{Im}\Sigma_{\alpha\beta}(v) &= -\pi U^2 \int dw dw' [A_{\alpha\beta}^-(w) A_{\alpha\beta}^+(w') A_{\alpha\beta}^-(v-w+w') \\ &\quad + A_{\alpha\beta}^+(w) A_{\alpha\beta}^-(w') A_{\alpha\beta}^+(v-w+w')], \end{aligned} \quad (\text{B10})$$

where

$$\begin{aligned} A_{\alpha\beta}^+(w) &= \theta(w) A_{\alpha\beta}(w) = -\theta(w) \text{Im}G_{\alpha\beta}^0(w)/\pi \\ &= \frac{1}{2} [\delta(w - t_\perp) + \delta(w + t_\perp)], \end{aligned} \quad (\text{B11a})$$

$$\begin{aligned} A_{\alpha\beta}^-(w) &= \theta(-w) A_{\alpha\beta}(w) = -\theta(-w) \text{Im}G_{\alpha\beta}^0(w)/\pi \\ &= \frac{1}{2} [\delta(w - t_\perp) - \delta(w + t_\perp)], \end{aligned} \quad (\text{B11b})$$

where $\theta(w)$ is the Heaviside step function. Replacing into Eq. (B10),

$$\begin{aligned} \text{Im}\Sigma_{11}(v) &= -\pi \frac{U^2}{4} \int dw dw' [\theta(-w) \delta(w + t_\perp) \theta(w') \\ &\quad \times \delta(w' - t_\perp) A^-(v-w+w') + \theta(w) \delta(w - t_\perp) \theta(-w') \\ &\quad \times \delta(w' + t_\perp) A^+(v-w+w')] \\ &= -\pi \frac{U^2}{4} \int dw' [\theta(w') \delta(w' - t_\perp) A^-(v + t_\perp + w') \\ &\quad + \theta(-w') \delta(w' + t_\perp) A^+(v - t_\perp + w')] \\ &= -\pi \frac{U^2}{4} [A^-(v + 2t_\perp) + A^+(v - 2t_\perp)] \\ &= -\pi \frac{U^2}{8} \{ \theta[-(v + 2t_\perp)] [\delta(v - t_\perp) + \delta(v + 3t_\perp)] \\ &\quad + \theta(v - 2t_\perp) [\delta(v - 3t_\perp) + \delta(v - t_\perp)] \}, \\ \text{Im}\Sigma_{11}(v) &= -\pi \frac{U^2}{8} [\delta(v + 3t_\perp) + \delta(v - 3t_\perp)]. \end{aligned} \quad (\text{B12})$$

The real part can be obtained by the Kramers-Kronig relation. A similar procedure is followed to find Σ_{12} , after which one recovers the exact expressions as presented in (B8). Thus, one can assert that the IPT approximation is exact in the zero-temperature and $t = 0$ limits.

- [1] I. H. Inoue and M. J. Rozenberg, Taming the Mott transition for a novel Mott transistor, *Adv. Funct. Mater.* **18**, 2289 (2008).
- [2] P. Stoliar, J. Tranchant, B. Corraze, E. Janod, M.-P. Besland, F. Tesler, M. Rozenberg, and L. Cario, A leaky-integrate-and-fire neuron analog realized with a Mott insulator, *Adv. Funct. Mater.* **27**, 1604740 (2017).
- [3] J. B. Goodenough, Direct cation-cation interactions in several oxides, *Phys. Rev.* **117**, 1442 (1960).
- [4] J. B. Goodenough, The two components of the crystallographic transition in VO₂, *J. Solid State Chem.* **3**, 490 (1971).
- [5] R. M. Wentzcovitch, W. W. Schulz, and P. B. Allen, VO₂: Peierls or Mott-Hubbard? A View from Band Theory, *Phys. Rev. Lett.* **72**, 3389 (1994).
- [6] V. Eyert, The metal-insulator transitions of VO₂: A band theoretical approach, *Ann. Phys. (NY)* **11**, 650 (2002).
- [7] S. Biermann, A. Poteryaev, A. I. Lichtenstein, and A. Georges, Dynamical Singlets and Correlation-Assisted Peierls Transition in VO₂, *Phys. Rev. Lett.* **94**, 026404 (2005).
- [8] J. M. Tomczak, F. Aryasetiawan, and S. Biermann, Effective band structure in the insulating phase versus strong dynamical correlations in metallic VO₂, *Phys. Rev. B* **78**, 115103 (2008).
- [9] Cédric Weber, D. D. O'Regan, N. D. M. Hine, M. C. Payne, G. Kotliar, and P. B. Littlewood, Vanadium Dioxide: A Peierls-Mott Insulator Stable against Disorder, *Phys. Rev. Lett.* **108**, 256402 (2012).
- [10] W. H. Brito, M. C. O. Aguiar, K. Haule, and G. Kotliar, Metal-Insulator Transition in VO₂: A DFT+DMFT Perspective, *Phys. Rev. Lett.* **117**, 056402 (2016).
- [11] V. Eyert, VO₂: A Novel View from Band Theory, *Phys. Rev. Lett.* **107**, 016401 (2011).
- [12] A. S. Belozerov, M. A. Korotin, V. I. Anisimov, and A. I. Poteryaev, Monoclinic M₁ phase of VO₂: Mott-Hubbard versus band insulator, *Phys. Rev. B* **85**, 045109 (2012).
- [13] Dušan Plašienka, R. Martoňák, and M. C. Newton, *Ab initio* molecular dynamics study of the structural and electronic transition in VO₂, *Phys. Rev. B* **96**, 054111 (2017).
- [14] O. Nájera, M. Civelli, V. Dobrosavljević, and M. J. Rozenberg, Resolving the VO₂ controversy: Mott mechanism dominates the insulator-to-metal transition, *Phys. Rev. B* **95**, 035113 (2017).
- [15] M. M. Qazilbash, M. Brehm, B.-G. Chae, P.-C. Ho, G. O. Andreev, B.-J. Kim, S. J. Yun, A. V. Balatsky, M. B. Maple, F. Keilmann *et al.*, Mott transition in VO₂ revealed by infrared spectroscopy and nano-imaging, *Science* **318**, 1750 (2007).
- [16] J. M. Tomczak and S. Biermann, Effective band structure of correlated materials: the case of VO₂, *J. Phys.: Condens. Matter* **19**, 365206 (2007).
- [17] Hyun-Tak Kim, Yong Wook Lee, Bong-Jun Kim, Byung-Gyu Chae, Sun Jin Yun, Kwang-Yong Kang, Kang-Jeon Han, Ki-Ju Yee, and Yong-Sik Lim, Monoclinic and Correlated Metal Phase in VO₂ as Evidence of the Mott Transition: Coherent Phonon Analysis, *Phys. Rev. Lett.* **97**, 266401 (2006).
- [18] E. Arcangeletti, L. Baldassarre, D. Di Castro, S. Lupi, L. Malavasi, C. Marini, A. Perucchi, and P. Postorino, Evidence of a Pressure-Induced Metallization Process in Monoclinic VO₂, *Phys. Rev. Lett.* **98**, 196406 (2007).
- [19] M. M. Qazilbash, A. Tripathi, A. A. Schafgans, Bong-Jun Kim, Hyun-Tak Kim, Zhonghou Cai, M. V. Holt, J. M. Maser, F. Keilmann, O. G. Shpyrko, and D. N. Basov, Nanoscale imaging of the electronic and structural transitions in vanadium dioxide, *Phys. Rev. B* **83**, 165108 (2011).
- [20] Zhensheng Tao, Tzong-Ru T. Han, Subhendra D. Mahanti, Phillip M. Duxbury, Fei Yuan, Chong-Yu Ruan, Kevin Wang, and Junqiao Wu, Decoupling of Structural and Electronic Phase Transitions in VO₂, *Phys. Rev. Lett.* **109**, 166406 (2012).
- [21] R. Yoshida, T. Yamamoto, Y. Ishida, H. Nagao, T. Otsuka, K. Saeki, Y. Muraoka, R. Eguchi, K. Ishizaka, T. Kiss *et al.*, Ultrafast photoinduced transition of an insulating VO₂ thin film into a nonrutile metallic state, *Phys. Rev. B* **89**, 205114 (2014).
- [22] V. R. Morrison, R. P. Chatelain, K. L. Tiwari, A. Hendaoui, A. Bruhács, M. Chaker, and B. J. Siwick, A photoinduced metal-like phase of monoclinic VO₂ revealed by ultrafast electron diffraction, *Science* **346**, 445 (2014).
- [23] J. Laverock, S. Kittiwatanakul, A. A. Zakharov, Y. R. Niu, B. Chen, S. A. Wolf, J. W. Lu, and K. E. Smith, Direct Observation of Decoupled Structural and Electronic Transitions and an Ambient Pressure Monocliniclike Metallic Phase of VO₂, *Phys. Rev. Lett.* **113**, 216402 (2014).
- [24] D. Wegkamp, M. Herzog, L. Xian, M. Gatti, P. Cudazzo, C. L. McGahan, R. E. Marvel, R. F. Haglund, A. Rubio, M. Wolf, and J. Stähler, Instantaneous Band Gap Collapse in Photoexcited Monoclinic VO₂ due to Photocurrent Doping, *Phys. Rev. Lett.* **113**, 216401 (2014).
- [25] Zenji Hiroi, Structural instability of the rutile compounds and its relevance to the metal-insulator transition of VO₂, *Prog. Solid State Chem.* **43**, 47 (2015).
- [26] A. Georges, G. Kotliar, W. Krauth, and M. J. Rozenberg, Dynamical mean-field theory of strongly correlated fermion systems and the limit of infinite dimensions, *Rev. Mod. Phys.* **68**, 13 (1996).
- [27] G. Moeller, V. Dobrosavljević, and A. E. Ruckenstein, RKKY interactions and the Mott transition, *Phys. Rev. B* **59**, 6846 (1999).
- [28] P. Werner and A. J. Millis, Hybridization expansion impurity solver: General formulation and application to Kondo lattice and two-orbital models, *Phys. Rev. B* **74**, 155107 (2006).
- [29] P. Seth, I. Krivenko, M. Ferrero, and O. Parcollet, TRIQS/CTHYB: A continuous-time quantum monte carlo hybridisation expansion solver for quantum impurity problems, *Comput. Phys. Commun.* **200**, 274 (2016).
- [30] The derivation of the R2B formulas and a study of the behavior of the self-energy in the low-frequency regime is presented in Appendix A.
- [31] H. Hafermann, M. I. Katsnelson, and A. I. Lichtenstein, Metal-insulator transition by suppression of spin fluctuations, *Europhys. Lett.* **85**, 37006 (2009).
- [32] A. Fuhrmann, D. Heilmann, and H. Monien, From Mott insulator to band insulator: A dynamical mean-field theory study, *Phys. Rev. B* **73**, 245118 (2006).
- [33] G. Mazza, A. Amaricci, M. Capone, and M. Fabrizio, Field-Driven Mott Gap Collapse and Resistive Switch in Correlated Insulators, *Phys. Rev. Lett.* **117**, 176401 (2016).

- [34] S. Doniach, The Kondo lattice and weak antiferromagnetism, *Phys. B+C (Amsterdam)* **91**, 231 (1977).
- [35] R. Bulla, A. C. Hewson, and Th. Pruschke, Numerical renormalization group calculations for the self-energy of the impurity Anderson model, *J. Phys.: Condens. Matter* **10**, 8365 (1998).
- [36] D. J. García, K. Hallberg, and M. J. Rozenberg, Dynamical Mean Field Theory with the Density Matrix Renormalization Group, *Phys. Rev. Lett.* **93**, 246403 (2004).
- [37] M. J. Rozenberg, G. Kotliar, and X. Y. Zhang, Mott-Hubbard transition in infinite dimensions. II, *Phys. Rev. B* **49**, 10181 (1994).